Ultratough graphene–black phosphorus films

Tianzhu Zhou[a,b,c,1], Hong Ni[a,1], Yanlei Wang[d,1], Chao Wu[b,1], Hao Zhang[e], Jianqi Zhang[f], Antoni P. Tomsia[c], Lei Jiang[a,c], and Qunfeng Cheng[a,c,g,2]

[a]Key Laboratory of Bio-inspired Smart Interfacial Science and Technology of Ministry of Education, School of Chemistry, Beihang University, Beijing 100191, People's Republic of China; [b]School of Transportation Science and Engineering, Beihang University, Beijing 100191, People's Republic of China; [c]Beijing Advanced Innovation Center for Biomedical Engineering, Beihang University-University of Wollongong (BUAA-UOW) Joint Research Centre, Beihang University, Beijing 100191, People's Republic of China; [d]Beijing Key Laboratory of Ionic Liquids Clean Process, Institute of Process Engineering, Chinese Academy of Sciences (CAS), Beijing 100190, People's Republic of China; [e]Beijing Key Laboratory of Advanced Chemical Energy Storage Technologies and Materials, Research Institute of Chemical Defense, Beijing 100191, People's Republic of China; [f]CAS Key Laboratory of Nanosystem and Hierarchical Fabrication, CAS Center for Excellence in Nanoscience, National Center for Nanoscience and Technology, Beijing 100190, People's Republic of China; and [g]School of Materials Science and Engineering, Zhengzhou University, Zhengzhou 450001, People's Republic of China

Edited by Peidong Yang, University of California, Berkeley, CA, and approved January 27, 2020 (received for review September 24, 2019)

Graphene-based films with high toughness have many promising applications, especially for flexible energy storage and portable electrical devices. Achieving such high-toughness films, however, remains a challenge. The conventional mechanisms for improving toughness are crack arrest or plastic deformation. Herein we demonstrate black phosphorus (BP) functionalized graphene films with record toughness by combining crack arrest and plastic deformation. The formation of covalent bonding P-O-C between BP and graphene oxide (GO) nanosheets not only reduces the voids of GO film but also improves the alignment degree of GO nanosheets, resulting in high compactness of the GO film. After further chemical reduction and π-π stacking interactions by conjugated molecules, the alignment degree of rGO nanosheets was further improved, and the voids in lamellar graphene film were also further reduced. Then, the compactness of the resultant graphene films and the alignment degree of reduced graphene oxide nanosheets are further improved. The toughness of the graphene film reaches as high as ∼51.8 MJ m^{-3}, the highest recorded to date. In situ Raman spectra and molecular dynamics simulations reveal that the record toughness is due to synergistic interactions of lubrication of BP nanosheets, P-O-C covalent bonding, and π-π stacking interactions in the resultant graphene films. Our tough black phosphorus functionalized graphene films with high tensile strength and excellent conductivity also exhibit high ambient stability and electromagnetic shielding performance. Furthermore, a supercapacitor based on the tough films demonstrated high performance and remarkable flexibility.

graphene | black phosphorus | film | mechanical properties

Graphene-based films with exceptional strength and excellent conductivity have been widely used in the fields of flexible energy storage and portable electrical devices (1–3). Recently, some representative methods have been reported to develop graphene-based films, including layer-by-layer deposition, evaporation, hydrogel casting, and electrophoretic deposition (4). However, it is difficult to design interfacial interactions between graphene nanosheets with these methods, resulting in films having poor stress transfer efficiency and low toughness. Like bulk materials, 2D films can achieve high toughness via the mechanism of crack arrest or plastic deformation (5). Recently, inspired by the hierarchical microscale/nanoscale structure and abundant interface interactions of natural nacre (6), various interfacial interactions, such as hydrogen bonding, ionic bonding, π-π stacking interactions, and covalent bonding, have been demonstrated to enhance the toughness of graphene-based films (7–10). These interfacial effects can not only inhibit the crack propagation of graphene films but also effectively improve their plastic deformation. Nevertheless, a great challenge remains: to improve the toughness of graphene films by integration of plastic deformation while at the same time inhibiting crack propagation.

Black phosphorus (BP) nanosheets, as a new 2D material with high charge carrier mobility and a unique band gap (11–14), have attracted a great deal of interest (15). Like sulfur, phosphorus (P) demonstrates a special lubricating property (16, 17). Inspired by the interfacial design of natural nacre, we fabricated BP functionalized graphene films. The combination of covalent bonding P-O-C between GO and BP nanosheets and π-π stacking interactions by the long-chain molecules (1-aminopyrene [AP]-disuccinimidyl suberate [DSS] [AD]) achieves interfacial synergistic effect in the rGO-BP-AD film, resulting in record toughness (∼51.8 MJ m^{-3}) with the high strain of ∼16.7%. Tensile strength and high conductivity were also achieved as high as ∼653.5 MPa and ∼493.5 S cm^{-1}, respectively. The ultrahigh toughness is due to the high degree of orientation and compactness of graphene nanosheets resulting from the synergistic effect. In situ Raman spectra and molecular dynamics simulations revealed that the record toughness of rGO-BP-AD film can be attributed to the synergistic effect from P-O-C covalent bonding between BP and GO nanosheets, lubrication of BP nanosheets, and π-π stacking interactions between AD molecules and rGO nanosheets. The mechanisms of crack arrest and plastic deformation for improving the toughness of our films are combined via this kind of synergistic effect. The rGO-BP-AD film also shows high electromagnetic interference (EMI) shielding (∼29.7 dB). The supercapacitor assembled using our rGO-BP-AD film

Significance

This manuscript describes the functionalization of the graphene oxide (GO) nanosheets by black phosphorus (BP) nanosheets through P-O-C covalent bonding. Such a strategy reduces the voids in the lamellar graphene film and makes the graphene film much more compact, while at the same time improving the alignment degree of GO nanosheets. Equally important, the conjugated AD molecules improve the compactness of the graphene films and the alignment degree of rGO nanosheets via π-π stacking interaction between adjacent rGO nanosheets. As a result, the record high toughness of our graphene film was achieved along with excellent electrical conductivity. In addition, our tough graphene–black phosphorus films also exhibit high ambient stability and electromagnetic shielding performance.

Author contributions: Q.C. designed research; T.Z., H.N., and J.Z. performed research; T.Z., H.N., Y.W., C.W., H.Z., J.Z., A.P.T., L.J., and Q.C. analyzed data; and T.Z., H.N., Y.W., A.P.T., L.J., and Q.C. wrote the paper.

Competing interest statement: Q.C. has filed a patent application related to this article.

This article is a PNAS Direct Submission.

[1]T.Z., H.N., Y.W., and C.W. contributed equally to this work.

[2]To whom correspondence may be addressed. Email: cheng@buaa.edu.cn.

This article contains supporting information online at https://www.pnas.org/lookup/suppl/doi:10.1073/pnas.1916610117/-/DCSupplemental.

First published April 6, 2020.

demonstrated remarkable flexibility with no decline of capacitance after 10,000 bending cycles at 180°.

The fabrication of bioinspired rGO-BP-AD film is illustrated in Fig. 1*A* and *SI Appendix*, Fig. S1. The GO nanosheets are assembled into resultant graphene film via vacuum assisted filtration and hydriodic acid (HI) reduction. The small-angle X-ray scattering (SAXS) was applied to obtain the porosity of resultant graphene films, as shown in Fig. 1 *B*–*D*. The scattering intensity of rGO-BP-AD film is decreased compared to that of rGO film. The porosity of the rGO-BP-AD film is only 4.9%, which is much lower than the pure GO film with porosity of 14.8%, as shown in Fig. 1*E*. This is because the small size BP nanosheets are attached on the surface of GO nanosheets through covalent bonding, filling the voids of the lamellar graphene film and making the graphene film much more compact (18). Moreover, the rGO-BP-AD film also shows high orientation, which is confirmed by the decrease in full width at half maximum (FWHM) in the wide-angle X-ray scattering (WAXS) pattern, as shown in Fig. 1 *F* and *G*. The FWHM of the rGO-BP-AD film is 25.6°, which is much lower than pure rGO film with 33.5°. This is because of the strong interfacial interactions, including P-O-C covalent bonding and π-π stacking interaction between rGO nanosheets and AD molecules. The GO nanosheet shows a thickness of ∼1.0 nm and lateral size of ∼15.0 μm (Fig. 1*H* and *SI Appendix*, Fig. S2 *A* and *B*). The exfoliated monolayer BP nanosheet thickness and lateral size (∼0.5 nm and ∼1.2 μm, respectively) were confirmed by atomic force microscopy (AFM) and scanning electron microscopy (SEM) (Fig. 1*I* and *SI Appendix*, Fig. S2 *C* and *D*). In addition, as presented in *SI Appendix*, Figs. S3 and S4, the lattice spacing of the exfoliated BP nanosheet is 0.22 nm with the expected (200), (101), and (002) planes confirmed by a high-resolution transmission electron microscope (HR-TEM), which verified that the BP nanosheet is a monolayer, consistent with previous reports (19). The BP and GO monolayer nanosheets in mixing solution reacted completely under ambient temperature, which was verified via the zeta potential (*SI Appendix*, Fig. S5). The BP functionalized GO

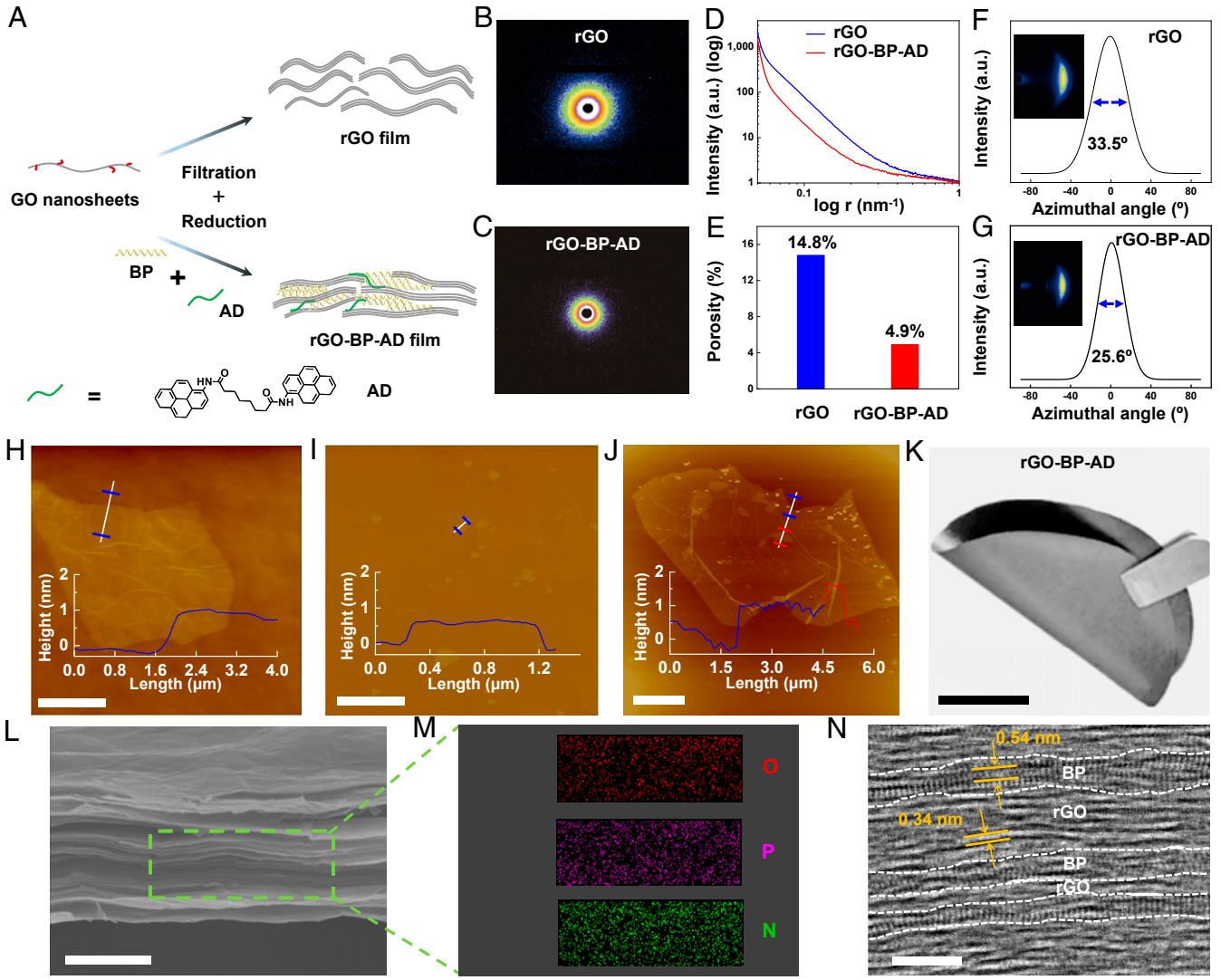

Fig. 1. Fabrication process of bioinspired rGO-BP-AD films. (*A*) Illustration of the manufacturing process of BP functionalized graphene films. SAXS patterns of (*B*) pure rGO and (*C*) rGO-BP-AD films. (*D*) Corresponding intensity curves according to the SAXS patterns. (*E*) Porosity of the pure rGO and rGO-BP-AD films. The WAXS patterns of (*F*) rGO and (*G*) rGO-BP-AD. AFM of (*H*) monolayer GO nanosheets, (*I*) BP nanosheets, and (*J*) covalently cross-linked GO-BP nanosheets. (Scale bar, 5 μm.) (*K*) A digital photograph of rGO-BP-AD. (Scale bar, 2 cm.) (*L*) SEM of cross-sectional view of rGO-BP-AD films. (Scale bar, 2 μm.) (*M*) EDS mapping of O, P, and N elements. (*N*) HR-TEM image of the cross-section of the bioinspired rGO-BP-AD films, which shows three to six layers of monolayer BP nanosheets with the d-spacing of 0.54 nm and rGO nanosheets with the d-spacing of 0.34 nm. (Scale bar, 5 nm.)

nanosheets (Fig. 1*J*) in the mixing solution were filtrated with the assistance of a vacuum to obtain the free-standing GO-BP film with stacking BP nanosheets in the layers of rGO nanosheets. After reduction by hydroiodic acid (HI), the reduced GO-BP (rGO-BP) films were immersed in the N,*N*-dimethyl formamide (DMF) solution with long-chain AD molecules, and then the rGO-BP-AD films were achieved via π-π stacking interactions of AD (Fig. 1*K*). The mapping of P and N elements in the cross-section of rGO-BP-AD film indicated uniform distribution of BP nanosheets and AD molecules, respectively, as shown in Fig. 1 *L* and *M*. Moreover, an HR-TEM image shows the alternatively layered structure with BP and rGO nanosheets, and several BP nanosheets stacked together into layers with thicknesses of 1.5 to 3.0 nm, as shown in Fig. 1*N* and *SI Appendix*, Fig. S6. The resultant GO-BP films with different weight ratios of BP nanosheets were prepared by the same method and termed as GO-BP-I, GO-BP-II, GO-BP-III, and GO-BP-IV. The other samples, such as GO, rGO, rGO-AD, and GO-BP-AD (the weight ratio of BP nanosheets and AD molecules is consistent with GO-BP-III and rGO-AD) films, were fabricated using the same approach. The precise weight of BP nanosheets in the GO-BP films was verified by thermogravimetry analysis (*SI Appendix*, Fig. S7), and the corresponding data are listed in *SI Appendix*, Table S1.

X-ray diffraction (XRD) patterns show that the typical characteristic peak of GO in GO-BP-III and GO-BP-AD at 2θ of ∼10.0° disappeared and emerged at 2θ of 22.81° and 22.24° as shown in Fig. 2*A* and *SI Appendix*, Fig. S8. This is due to in situ reduction of GO by BP nanosheets. In addition, GO-BP-III and GO-BP-AD films show lower d-spacing of 3.91 and 4.15 Å, respectively, lower than the pure GO film with d-spacing of 7.50 but a little higher than HI chemically reduced rGO-BP-III and rGO-BP-AD films with d-spacing of 3.72 and 3.91 Å, respectively. These results indicate the GO nanosheets are partly reduced by BP nanosheets via the removal of oxygen-containing functional groups. Fourier transform infrared spectrometry (FTIR) spectra show that the new peak appeared at a wavenumber of ∼1,010 cm^{-1} for rGO-BP-III and rGO-BP-AD films, indicating the formation of P-O-C covalent bonding between BP and rGO nanosheets (20), as shown in Fig. 2*B* and *SI Appendix*, Fig. S9. Moreover, some new characteristic peaks at wavenumbers of ∼1,252, ∼1,526, and ∼1,655 cm^{-1} for rGO-BP-AD films are assigned to functional group -NH- and -C=O of the AD molecules compared with rGO-BP-III films, indicating that AD molecules have successfully chemically cross-linked with rGO nanosheets via π-π stacking interactions (21).

Raman spectra show that the in-plane A_g^2 of exfoliated BP nanosheets has shifted to a higher wavenumber due to phonon confinement, indicating the monolayer BP (22), as shown in *SI Appendix*, Fig. S10*A*. The ratio of I_D to I_G for GO-BP-III increased to 1.3 as compared with the pure GO with the ratio of 0.9, indicating GO nanosheets were reduced by BP nanosheets (23), as shown in Fig. 2*C*. After reduction, the ratio of I_D to I_G for rGO-BP-AD and rGO-BP-III films increased to about 1.5, which is due to the reduction by BP and HI. In addition, the peak of G band for GO-BP-III films at 1,604 cm^{-1} has shifted 18 cm^{-1} as compared with that of pure GO film at 1,586 cm^{-1} (*SI Appendix*, Fig. S10*B*), indicating the formation of P-O-C covalent bonding between BP and GO nanosheets (24). X-ray photoelectron spectroscopy (XPS) spectra (*SI Appendix*, Fig. S11*A*) revealed that the BP nanosheets and AD molecules had been successfully introduced into the layer of rGO nanosheets according to the appearance of P and N elements in rGO-BP-AD films. Moreover, the intensity ratio of I_{C1s} to I_{O1s} of GO-BP-III increased to 1.45 compared with GO films with the ratio of 0.62 (*SI Appendix*, Table S3). The ratio of rGO-BP-III reached up to 5.20, consistent with that of rGO-BP-AD (5.22), due to the reduction of GO by BP and HI. P 2p spectra of BP nanosheets (Fig. 2*D* and *SI Appendix*, Fig. S11*B*) show that the two typical peaks at 130.0 and 130.9 eV belong to P-P bonds of P $2p_{3/2}$ and P $2p_{1/2}$ (22), respectively. When BP nanosheets have been successfully introduced into the layers of the GO nanosheets to obtain GO-BP-III films, the increasing proportion of PO_x for GO-BP-III films is attributed to the P-O-C covalent bonding (17) between BP and GO nanosheets, consistent with the results of FTIR and Raman spectra.

Subsequently, ^{31}P solid-state NMR (SNMR) and UV-vis spectroscopy were further employed to study the bonding structure of BP and GO nanosheets. The characteristic peak at 21.9 ppm in BP nanosheets shifted to 20.2 ppm in the spectrum of GO-BP-III film, indicating a shielding effect with an increasing electron density of the nucleus of O atom due to the P-O-C covalent bonding between BP and GO nanosheets, as shown in Fig. 2*E*. There are several new peaks at 8.8, 5.7, and 1.4 ppm (15) in the GO-BP-III film. They are probably due to the functionalized P-O-C covalent bonding between BP and GO nanosheets, leading to the low crystallinity of BP nanosheets (25). The comparison of UV-vis spectra of the BP, GO, and GO-BP-III films is shown in Fig. 2*F*. The observed signal peaks at 230 and 300 nm are assigned to π-π* transition of the C=C and n-π* transition of the carboxyl functional group (26) of GO spectra. When BP nanosheets were introduced into the layer of GO nanosheets, the typical peak at wavenumber of 230 nm showed red-shift to 250 nm. The shoulder peak at about 300 nm disappeared. The obtained results confirm the reduction with BP nanosheets and the formation of P-O-C covalent bonding between BP and GO nanosheets, consistent with the aforementioned characterizations. Therefore, the P-O-C covalent bonding between BP and GO nanosheets is possibly formed via nucleophilic substitution (*SI Appendix*, Fig. S12). The functional group of $-C{=}OH^+$ and $-C{-}OH_2^+$ is first formed with H^+ ion in solution due to the abundant oxygen-containing functional group (-COOH and -OH) of GO nanosheets. As the reaction continues, the in situ formed $BP{-}O^-$ in solution attack the C of $-C{=}OH^+$ and $-C{-}OH_2^+$, resulting in the removal of H_2O from the GO nanosheets. Finally, the P-O-C covalent bonding is formed, leading to the reduction of GO nanosheets (22).

The stress–strain curves are shown in Fig. 3 *A* and *B* and *SI Appendix*, Fig. S13. Pure GO film shows a low tensile strength of 91.4 ± 8.8 MPa, strain of 2.6 ± 0.2%, and toughness of 1.3 ± 0.1 MJ m^{-3} due to the weak interfacial reaction between GO nanosheets. When BP nanosheets are introduced, the obtained GO-BP-III film shows a tensile strength of 208.7 ± 11.0 MPa and toughness of 7.1 ± 0.2 MJ m^{-3}, which are 2.3 times and 5.5 times higher than pure GO film. This may be due to the P-O-C covalent bonding between BP and GO nanosheets and lubrication of BP nanosheets. After reduction by HI, the tensile strength of rGO-BP-III film reaches up to 296.1 ± 9.5 MPa with the strain of 12.6 ± 0.7% and high toughness of 15.6 ± 0.7 MJ m^{-3}. The tensile strength and toughness are 1.9 times and 2.6 times higher than that of GO-BP-III. The rGO-BP-AD film shows the tensile strength of 653.5 ± 21.4 MPa with the strain of 16.7 ± 0.3% and toughness of 51.8 ± 2.7 MJ m^{-3}; the toughness is 20.7 times higher than pure rGO film. This record high toughness of rGO-BP-AD film is attributed to the interfacial synergetic interactions of BP, rGO nanosheets, and AD molecules. Furthermore, the weight ratio of monolayer BP also influences the tensile strength and toughness of the bioinspired film. *SI Appendix*, Fig. S14, shows that the GO-BP-III and rGO-BP-III films demonstrate the highest tensile strength and toughness with the content of 8.2 wt % BP nanosheets (*SI Appendix*, Table S1). When the content of BP is lower than 8.2 wt %, the rGO-BP film shows low tensile strength and toughness due to the unsaturated interaction between BP and GO nanosheets. With higher BP content than 8.2 wt %, such a large number of BP nanosheets in the layers of GO nanosheets hampers the dissipation of stress transfer when loading, thus also resulting in low tensile strength and toughness. The corresponding curves and detailed data of tensile strength and toughness are listed in *SI Appendix*, Fig. S14 and Table S4.

For comparison, we also prepared graphene–BP film through adding multilayer BP crystals, or a mixture of single layers and multilayers for comparing their mechanical properties. When the multilayer BP crystals or a mixture of single layers and

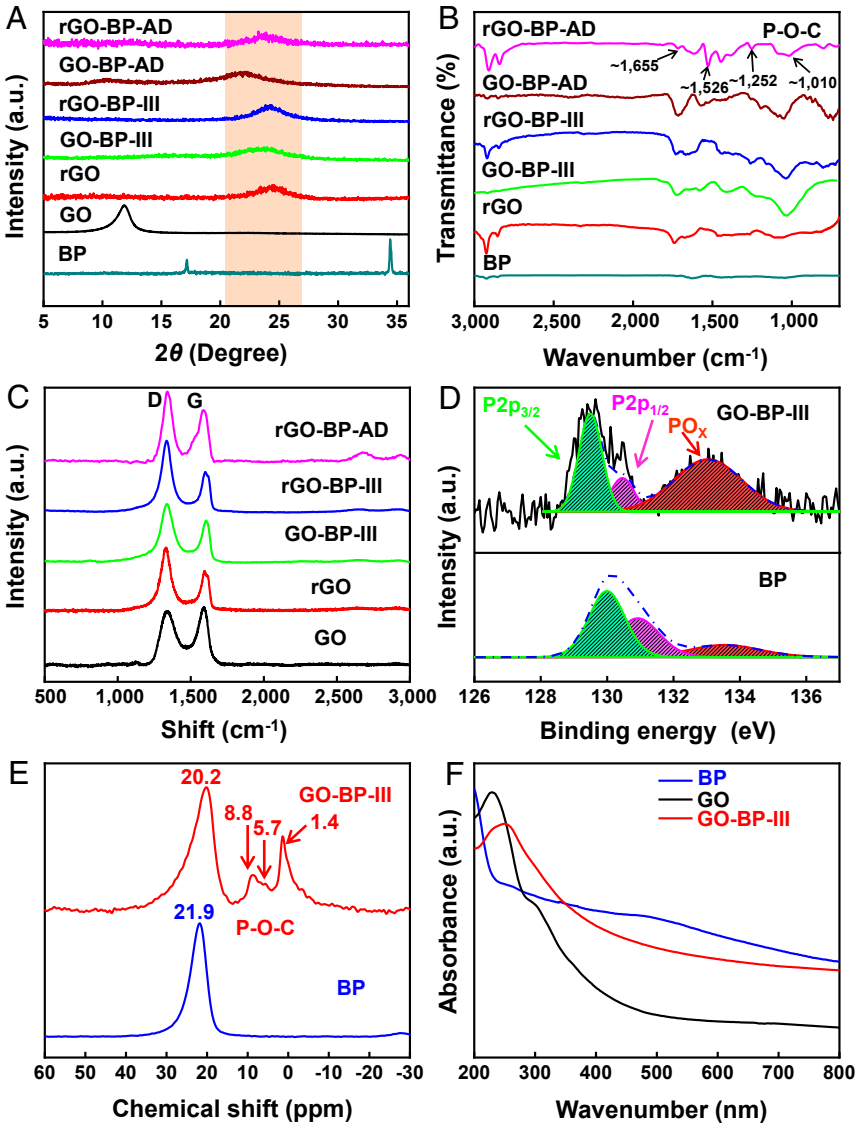

Fig. 2. Physical characterization and interaction of the bioinspired films. (*A*) XRD patterns. (*B*) FTIR spectra comparison of BP nanosheets, pure GO, rGO, GO-BP-III, rGO-BP-III, GO-BP-AD, and rGO-BP-AD films. (*C*) Raman spectra of obtained films. (*D*) XPS P 2p spectra of BP nanosheets and GO-BP films, which indicate the formation of P-O-C covalent bonding between BP nanosheets and GO nanosheets. (*E*) The ^{31}P SNMR spectra of BP nanosheets and bioinspired GO-BP-III films. Spectra demonstrate that the signal peak at 21.9 ppm presented in BP nanosheets shifts to 20.2 ppm for the GO-BP-III films, which indicates the formation of P-O-C covalent bonding between BP nanosheets and GO nanosheets. (*F*) UV-vis absorption spectra of BP nanosheets, pure GO film, and GO-BP-III films, suggesting that the GO nanosheets are reduced by BP nanosheets during the formation of P-O-C covalent bonding.

multilayers were added, the dispersity of solution is poorer than addition of single-layer BP sheets. According to the AFM image in *SI Appendix*, Fig. S15, the thickness of multilayer BP crystals is ∼5 nm, which is about 10 layers of BP nanosheets. Moreover, two graphene–BP films including multilayer BP crystals (named as rGO-mBP-III) or a mixture of single layers and multilayers (weight ratio of 1:1) (named as rGO-hBP-III) were prepared through same fabrication process. The obtained samples were then cross-linked with AD molecules into rGO-mBP-AD and rGO-hBP-AD film, respectively. The stress–strain curves and fracture morphology of rGO-mBP-AD and rGO-hBP-AD films are shown in *SI Appendix*, Figs. S16 and S17. The tensile strength and toughness of rGO-mBP-AD and rGO-hBP-AD, listed in *SI Appendix*, Table S4, are ∼242.2 and ∼503.1 MPa and 4.4 and 10.4 MJ m^{-3}, respectively. The toughness and tensile strength are lower than rGO-BP-AD film with tensile strength of ∼653.5 MPa and toughness of ∼51.8 MJ m^{-3}.

The study of the ambient stability of GO-BP-III film is first conducted by analyzing UV-vis spectra for 7 and 14 d in ambient atmosphere at room temperature as shown in *SI Appendix*, Fig. S18. When the GO-BP-III film is kept in the ambient atmosphere for 14 d, the UV-vis spectra are consistent with fresh GO-BP-III film. However, pure BP nanosheets easily suffered from the oxidation degradation, according to the characteristic peak at 468 nm which disappeared after 7 d in the atmosphere at room temperature. However, the mechanical properties of the rGO-BP-III and rGO-BP-AD films did not change. In addition, the XPS spectra of rGO-BP-III and rGO-BP-AD films were obtained after 40 d in the atmosphere at room temperature (*SI Appendix*, Fig. S19). The results show that the atoms ratio of P 2p$_{3/2}$, P 2p$_{1/2}$, and PO$_x$ was almost kept constant, similar to the fresh samples (*SI Appendix*, Table S5). The tensile strength of the rGO-BP-III and rGO-BP-AD films was still kept at ∼275.0 and ∼622.1 MPa after 14 d (Fig. 3*C*). The retention rate of toughness was up to ∼104.5 and ∼95.4%, with

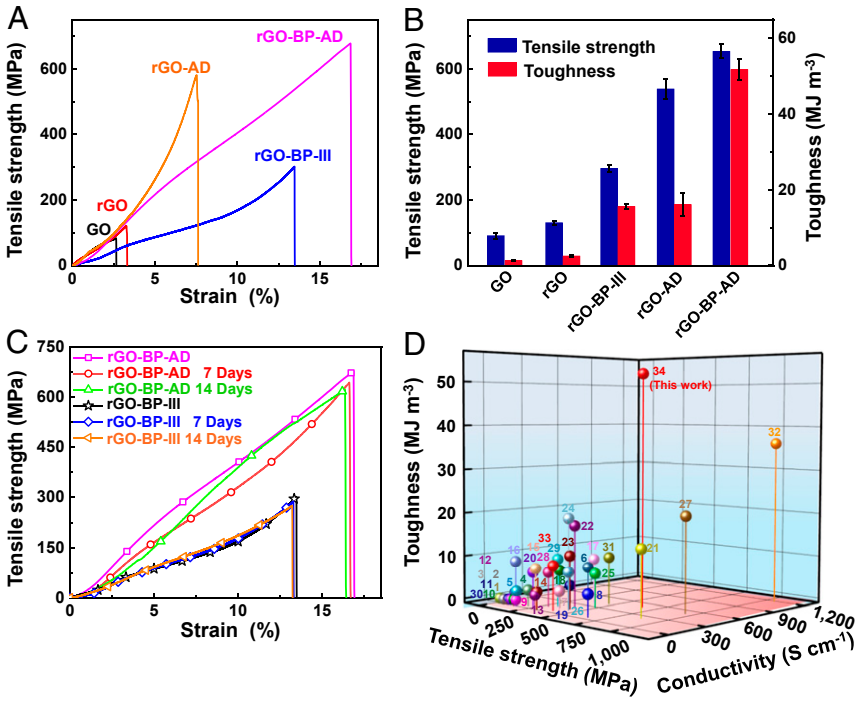

Fig. 3. Mechanical characterization of the bioinspired films. (*A*) Typical tensile strength curves. (*B*) Comparison of tensile strength and toughness of obtained bioinspired films. (*C*) Tensile strength of ambient stability of prepared rGO-BP-III and rGO-BP-AD films. (*D*) Comparison of tensile strength, toughness, and electrical conductivity of the nacre-inspired BP functionalized graphene films and other two or ternary graphene-based films.

the toughness of ~16.3 and ~9.4 MJ m^{-3}. The results further confirm that the formation of P-O-C covalent bonding could prevent oxidation of the BP nanosheets and improve their ambient stability. The water stability of pure GO, rGO, GO-BP-III, rGO-BP-III, GO-BP-AD, and rGO-BP-AD films was tested as shown in *SI Appendix*, Figs. S20 and S21, which is treated by ultrasonic processing (100 W, 4.5 KHz) for 0 to 8 h. The pure GO film disintegrates on hydration suffered from ultrasonic processing for 5 min and is completely redispersed after 1 h. However, GO-BP-III and GO-BP-AD films start to disintegrate after ultrasonic treatment for 1 and 1.5 h, respectively. Moreover, rGO film disintegrates after ultrasonic treatment for 3 h, while the rGO-BP-AD film remains intact in water suffer from ultrasonic processing for 8 h. Therefore, the water stability of rGO-BP-AD and GO-BP-AD film is superior to pure rGO and GO films.

Our bioinspired films show excellent electrical conductivity (*SI Appendix*, Table S6) due to a special electronic transmission channel between BP and GO nanosheets (23). With increasing content of BP nanosheets, the GO-BP film shows increased electrical conductivity from 8.5 ± 0.6 up to 22.7 ± 0.03 S cm^{-1}, which is due to the reduction of BP nanosheets inside GO nanosheets and the contribution of the interfacial reactions. These results are consistent with the data obtained by XRD, Raman, and UV-vis spectra. After reduction, the electrical conductivity of rGO-BP film improved to 367.1 ± 10.3 S cm^{-1}. These results further prove that the GO nanosheets are partly reduced by BP nanosheets. Furthermore, the rGO-BP-AD film shows electrical conductivity up to 493.5 ± 15.2 S cm^{-1}, which is 2.2 times higher than pure rGO film. In addition, our rGO-BP-AD film shows high thermal conductivity of 50.6 W m^{-1} K^{-1}, higher than that of rGO with the thermal conductivity of 22.7 W m^{-1} K^{-1}. This is due to the synergistic interactions of the P-O-C covalent bonding between BP and rGO nanosheets and the π-π stacking interactions between AD molecules and rGO nanosheets, which accelerate electron transport (22). The comparison of the resultant graphene–BP film with other reported graphene-based films is listed in Fig. 3*D*. As presented in the image of comparison, our rGO-BP-AD film demonstrates a record toughness of ~51.8 MJ m^{-3}, higher than any other reported graphene-based films (27–53). The corresponding tensile strength, toughness, and electrical conductivity are listed in *SI Appendix*, Table S7.

To further investigate the toughening mechanism of the resultant bioinspired graphene films, in situ Raman spectra were conducted as shown in Fig. 4 *A*–*D*. The down-shift of G-band frequency of graphene was utilized to detect the load transfer efficiency (49). There is only 1.3 cm^{-1} G-band shift for pure rGO film at the strain of 0 to 2.0%, indicating weak interfacial interactions (Fig. 4*A*). The π-π stacking interactions between AD molecules and rGO show continuous load transfer at the strain of 0 to 7.0%, contributing to the arrest of the propagating crack (Fig. 4*B*). The G-band shifts continuously and reaches 7.8 cm^{-1} without a plateau, resulting in an uninterrupted increase of the load transfer efficiency. Interestingly, the G-band shift of rGO-BP-III increases to 2.2 cm^{-1} at the strain of 1.8% and stops for a plateau at the strain of 7.6% (Fig. 4*C*). Then, the G-band shifts further increases to 4.0 cm^{-1} at a strain of 9.5%. This unique G-band shift plateau starts from a strain of 1.8 to 7.6%, indicating the lubrication of stacked BP nanosheets that results in plastic deformation. Strong P-O-C covalent bonding between rGO nanosheets and BP nanosheets further enhances the G-band shift from 2.2 to 4.0 cm^{-1} until fracture. When introducing the combination of π-π stacking interactions and covalent bonding together in rGO-BP-AD, the synergistic effect is achieved, resulting in continuous improvement of the G-band shift to 15.3 cm^{-1} at a strain of 12.5% until break of the whole process of crack propagation (Fig. 4*D*). Then the tensile strength and the toughness of rGO-BP-AD are simultaneously enhanced.

Recently, the degree of orientation of graphene nanosheets, via fluidics-enabled assembly process or the introduction of π-π stacking interactions and covalent bonding into the graphene films with external molecules, has been enhanced to achieve high tensile strength and toughness of graphene-based films (53, 54). The orientation of the resultant films was investigated by WAXS (*SI Appendix*, Fig. S22), which shows a decrease of FWHM of the obtained azimuthal from 33.5° for the pure rGO films to 26.1° for

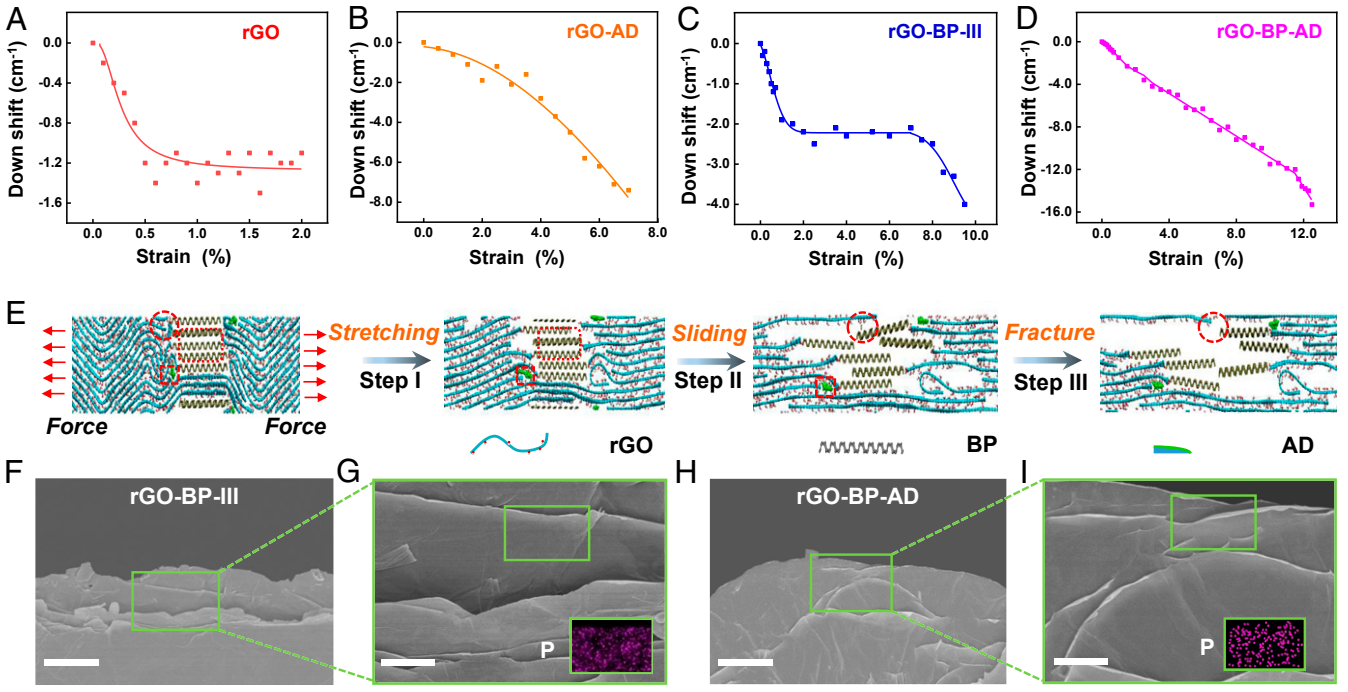

Fig. 4. Toughening mechanism of the bioinspired rGO-BP-AD films. (*A–D*) In situ Raman spectra of down shifts of graphene G-band frequency when gradually applying strain until fracture. (*E*) Molecular dynamics simulation for the proposed fracture mechanism of rGO-BP-AD films. (*F–I*) Fracture morphology of side view of rGO-BP-III and rGO-BP-AD films. (*Insets*) EDS of elemental P. (Scale bar, 5 μm [*F* and *H*] and 2 μm [*G* and *I*].)

rGO-AD, 26.4° for rGO-BP-III film, and 25.6° for rGO-BP-AD film. According to WAXS patterns, the obtained rGO-AD, rGO-BP-III, and rGO-BP-AD films show a high degree of orientation of 85.5, 85.3, and 85.8% compared with that of 81.4% of rGO films, as shown in *SI Appendix*, Table S8. Moreover, the degree of the orientation of rGO-BP-AD films is much higher than that of pure rGO, rGO-AD, and rGO-BP-III. According to a recent reported work (55), a mechanically strong graphene fiber could be fabricated to promote the fiber compactness via intercalating small-sized GO nanosheets into large-sized GO nanosheets. The compacted and oriented fibers result in the decline of porosity to achieve high mechanical strength and high thermal conductivity (55, 56). Therefore, when we introduce small-sized BP nanosheets (~1.2 μm) into the large-sized GO nanosheets (~15.0 μm) (*SI Appendix*, Fig. S2), the porosity of the resultant films is also reduced according the SAXS patterns (*SI Appendix*, Fig. S23). The porosity of rGO-BP-III film decreased to 5.8% with the introduction of BP nanosheets, indicating that the small BP nanosheets fill the space and voids and make the films more compact. The rGO-BP-AD film shows the lowest porosity with only 4.9%, which is attributed to the synergistic interaction of BP nanosheets and AD molecules, further condensing the resultant films. As a result, highly oriented and compacted rGO-BP-AD films via interfacial synergistic interaction achieve ultrahigh toughness of ~51.8 MJ m^{-3} and high tensile strength of ~653.5 MPa.

Molecular dynamics simulation was further applied to reveal the synergetic toughening mechanism. As shown in Fig. 4*I* and *SI Appendix*, Fig. S24, compared with the rGO-BP and rGO-AD films, the rGO-BP-AD films exhibit a unique synergetic toughening process: a plastic deformation process assisted by the lubrication of BP nanosheets (elliptical region), inhibiting the crack propagation process of π-π stacking interactions between AD molecules and rGO nanosheets (square region) and bridging of P-O-C covalent bonding between BP and rGO nanosheets (circular region). When the stretching procedure starts, the microcracks of adjacent rGO nanosheets have been initiated by the breakage of weak interactions along with mutual sliding of the rGO nanosheets (step I). According to the first-principle calculations in *SI Appendix*, Figs. S25 and S26, the energy barrier for the BP/BP interface (9.78 kcal mol^{-1} nm^2) is lower than that of the BP/GO interface (14.74 kcal mol^{-1} nm^2). This indicates the BP nanosheets slide against each other first, and then P-O-C covalent bonding breaks. Therefore, with increased loading to stretch the film, the BP nanosheets slide against each other due to the lubrication of BP nanosheets when the strong P-O-C covalent bonding is bridged with rGO nanosheets. The plastic deformation mainly arises from the lubrication of BP nanosheets, which is consistent with the result of G-band shift (Fig. 4*C*). Meanwhile, the long-chain AD molecules cross-linking with rGO nanosheets via π-π stacking interactions are stretched and further arrest the crack propagation before final fracture. Then, the BP nanosheets are separated from each other, and the π-π stacking interactions are broken (step II). With further stretching, the P-O-C covalent bonding between BP nanosheets and rGO nanosheets is broken; thus, it is difficult to arrest the crack propagation, and the complete fracture of films occurs (step III) (*SI Appendix*, Fig. S27). The fracture morphology of rGO-BP-III film shows a smooth curvature of rGO nanosheets (Fig. 4 *F* and *G*), while the rGO-BP-AD film presents curled edges after the pull-out of rGO nanosheets (Fig. 4 *H* and *I*) due to strong synergistic interactions. The P element mapping by elemental spectral analysis (EDS) characterization (Fig. 4 *G* and *I*, *Insets*) verified the BP nanosheets on the surface of pulled rGO nanosheets due to strong covalent bonding. The corresponding fracture morphologies of other films are listed in *SI Appendix*, Figs. S28 and S29.

In situ Raman frequency shifts during the loading–unloading process were also studied as shown in *SI Appendix*, Fig. S30. The reversible Raman frequency shifts of the G-band were observed for all films when the applied strain was lower than ~0.35%, which is attributed to the elastic deformability owing to the straightening of rGO nanosheets. Moreover, the strain-evoked reversible Raman frequency shifts without hysteresis have occurred for strains down to ~4.9% for rGO-AD elongated to ~5.6%, for strains down to ~5.8% for rGO-BP-III elongated to ~7.5%, and for strains down to ~8.5% for rGO-BP-AD elongated

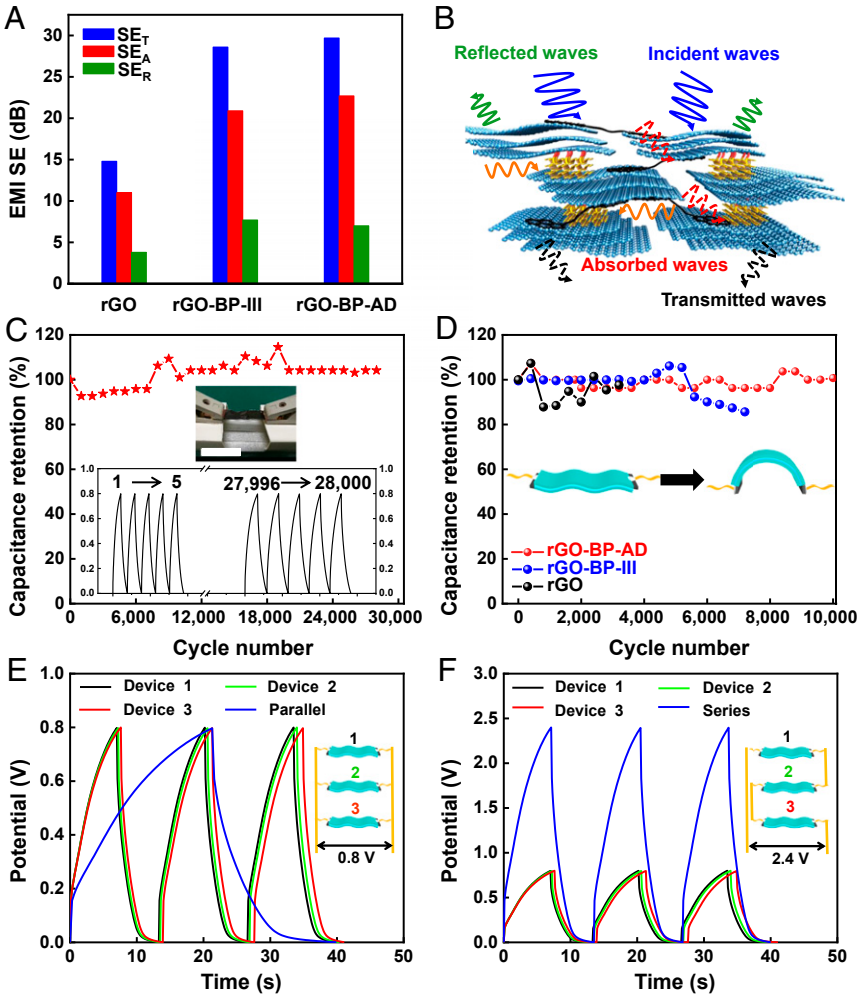

Fig. 5. EMI SE and electrochemical characterizations of the bioinspired films. (*A*) Total EMI SE (EMI SE_T), its absorption (SE_A), and its reflection (SE_R) at 8.0 GHz of pure rGO, rGO-BP-III, and rGO-BP-AD films at a thickness of ~5 μm. (*B*) Proposed EMI shielding mechanism. (*C*) Cycling life of FASs based on rGO-BP-AD films after 28,000 cycles according to the GCD curves at the current density of 4 A g^{-1}. (Scale bar, 2 cm.) (*D*) Capacitance retention of FASs based on pure rGO, rGO-BP-III, and rGO-BP-AD films when subjected to a bending state of 180° after 3,000 to 10,000 cycles according to the CV curves at a scan rate of 50 mV s^{-1}. (*E* and *F*) GCD curves in parallel and in series, respectively. (*Insets*) The schematic and equivalent circuit.

to ~10.5%. However, at a higher-strain region, no significant reversible shifts without hysteresis were observed for the strain-evoked downshift of the pure rGO films during the loading–unloading procedure. This generated elastic behavior at a high-strain region, when the loading applied to the graphene platelets, is possibly attributed to the elastic strain release because of the P-O-C covalent bonding, lubrication of BP nanosheets, π-π stacking interactions, or synergistic interactions.

Our ultratough BP functionalized graphene films also show other excellent properties, including EMI shielding (EMS SE). Fig. 5*A* and *SI Appendix*, Fig. S31, show the corresponding total shielding effectiveness (SE_T), absorption shielding effectiveness (SE_A), and reflection shielding effectiveness (SE_R) of the pure rGO, rGO-BP-III, and rGO-BP-AD films with the thickness of ~5 μm. The SE_T of rGO-BP-AD and rGO-BP-III has reached 29.7 and 28.6 dB at the frequency of 8.0 GHz, which is 2 times better than that of pure rGO film (14.8 dB). Moreover, the SE_A of rGO-BP-AD and rGO-BP-III reached 22.7 and 20.9 dB, which are 2 and 1.9 times better than that of pure rGO film (11.0 dB), respectively. Furthermore, all of the tested SE_A was higher than the SE_R, which means that the shielding dominant mechanism is attributed to the absorption rather than reflection. The proposed EMI shielding mechanism is described in Fig. 5*B* as the laminated shielding materials (57). When the initial electromagnetic waves (EMWs) strike the surface of the resultant graphene-based films, some EMWs are promptly reflected due to abundant free electrons on the surface of highly conductive rGO nanosheets. Sequentially, the residual EMWs pass through the lattice of BP nanosheets, resulting in significant decline in energy of the EMWs because of the developed electron density of BP nanosheets. Moreover, the surviving EMWs would encounter the next barrier layer of rGO nanosheets, and the attenuation of EMWs repeats. As a result, the EMWs could be reflected and absorbed back and forth between the layers. Therefore, the high EMI SE was reached via the bioinspired alternant laminated structure and synergistic interactions.

Finally, the ultratough BP functionalized graphene films were also assembled into the flexible all-solid-state supercapacitors (FASs) using PVA/H_3PO_4 as gel electrolyte. The rGO-BP-AD and rGO-BP-III films perform at much higher capacity than the pure rGO films according to the cyclic voltammetry (CV) curves at the scan rate of 10 mV s^{-1} (*SI Appendix*, Fig. S32*A*), which is attributed to the inserted BP nanosheets preventing aggregation of rGO nanosheets and interfacial synergistic interactions promoting energy storage. Meanwhile, CV curves of the rGO-BP-AD film at scan rates from 10 to 300 mV s^{-1} show no obvious distortion, as shown in *SI Appendix*, Fig. S32*B*, which indicates the good rate

capability for the rGO-BP-AD film (58). Moreover, the FASs based on rGO-BP-AD and rGO-BP-III both show ultralong cycling stability with the capacitance retention of ~100% after 28,000 (Fig. 5*C*) and 18,000 (*SI Appendix*, Fig. S33*A*) charge–discharge cycles according to the galvanostatic charge–discharge (GCD) curves at a current density of 4 A g^{-1}. Furthermore, the CV curves of FASs based on rGO-BP-AD show no fluctuations when bending from 0° to 180° (*SI Appendix*, Fig. S33*B*). Furthermore, Fig. 5*D* shows that the FASs based on rGO-BP-AD retain remarkable dynamic mechanical stability with ~100% retention of capacitance when bending at 180° after 10,000 cycles compared with ~97.6% retention after 3,200 cycles for pure rGO and ~85.6% retention after 7,200 cycles for rGO-BP-III followed by destruction. The obtained excellent cycling stability and exceptional mechanical flexibility are ascribed to the synergetic interactions of P-O-C covalent bonding, lubrication, and π-π stacking interaction. To make the material more practical for application, we also investigated FASs assembled in series or in parallel to satisfy the power and energy requirements through adjusting the discharge time and voltage window (59–61). As shown in Fig. 5 *E* and *F*, the same size FASs have been connected in parallel and in series. The in-parallel connecting FASs enhance the discharge time three times more than that of a single FASs with the same current density (Fig. 5*E*). Compared with the voltage window of 0.8 V of a single FASs, the voltage window of three connecting in-series FASs increases to 2.4 V with almost the same discharge time presented in Fig. 5*F*. Therefore, the ultratough BP functionalized graphene films present the potential for practical application in flexible energy storage devices.

Conclusion

We have successfully fabricated an ultratough BP functionalized graphene film inspired by natural nacre. The BP nanosheets not only partly reduce the GO nanosheets through P-O-C covalent bonding but also fill the voids of resultant graphene film, making the graphene film much more compact as well as improving the alignment degree of rGO nanosheets in the resultant graphene film. Meanwhile, the π-π stacking interaction between AD molecules and rGO nanosheets also reduces the porosity of graphene film and enhances the alignment degree of rGO nanosheets. The synergistic toughening effect from P-O-C covalent bonding, lubrication of BP nanosheets, and π-π stacking interaction between AD molecules and rGO nanosheets results in a record toughness of ~51.8 MJ m^{-3}, high tensile strength, and excellent electrical conductivity of films. Meanwhile, the synergistic interactions simultaneously enhance the electrical properties of the graphene films. The synergistic effect was verified by in situ Raman spectra and molecular dynamics simulations, which show the combination of crack arrest and plastic deformation. The ultratough BP functionalized graphene film also shows high EMI shielding performance and demonstrates excellent performance when used for FASs supercapacitors.

Materials and Methods

GO nanosheets suspension was obtained via modified Hummer's method. BP crystal was purchased from Xianfeng Technology Co. Ltd. The 1-Aminopyrene (AP) and disuccinimidyl suberate (DSS) were both obtained from Sigma-Aldrich Co. Ltd. The solution of hydroiodic acid (HI, 57 wt %) was obtained from Sigma-Aldrich Co. Ltd. All of the materials were used with no further purification. More details on the materials and methods can be found in *SI Appendix*.

Data Availability. All data are included in the manuscript and *SI Appendix*.

ACKNOWLEDGMENTS. This work was supported by the Excellent Young Scientist Foundation of the National Natural Science Foundation of China (NSFC) (Grant 51522301); the NSFC (Grants 51961130388, 21875010, 21273017, 51103004, and 51608020); Newton Advanced Fellowship (Grant NAF\R1\191235); Beijing Natural Science Foundation (Grant JQ19006); the 111 Project (Grant B14009); the Thousand Talents Plan (Young Professionals); the State Key Laboratory for Modification of Chemical Fibers and Polymer Materials, Donghua University (Grant LK1710); and the Fundamental Research Funds for the Central Universities (Grant YWF-19-BJ-J-8).

1. J. A. Rogers, T. Someya, Y. Huang, Materials and mechanics for stretchable electronics. *Science* **327**, 1603–1607 (2010).
2. R. O. Ritchie, The conflicts between strength and toughness. *Nat. Mater.* **10**, 817–822 (2011).
3. C. Luo, L. Zhou, K. Chiou, J. Huang, Multifunctional graphene hair dye. *Chem* **4**, 784–794 (2018).
4. S. Wan, J. Peng, L. Jiang, Q. Cheng, Bioinspired graphene-based nanocomposites and their application in flexible energy devices. *Adv. Mater.* **28**, 7862–7898 (2016).
5. C. Cao *et al.*, Nonlinear fracture toughness measurement and crack propagation resistance of functionalized graphene multilayers. *Sci. Adv.* **4**, eaao7202 (2018).
6. U. G. Wegst, H. Bai, E. Saiz, A. P. Tomsia, R. O. Ritchie, Bioinspired structural materials. *Nat. Mater.* **14**, 23–36 (2015).
7. Y. Zhang *et al.*, Graphene-based artificial nacre nanocomposites. *Chem. Soc. Rev.* **45**, 2378–2395 (2016).
8. Y. Zhou *et al.*, A printed, recyclable, ultra-strong, and ultra-tough graphite structural material. *Mater. Today* **30**, 17–25 (2019).
9. R. Soler-Crespo *et al.*, Atomically thin polymer layer enhances toughness of graphene oxide monolayers. *Matter* **1**, 369–388 (2019).
10. C. N. Yeh *et al.*, Binder-free graphene oxide doughs. *Nat. Commun.* **10**, 422 (2019).
11. X. Zhu *et al.*, Stabilizing black phosphorus nanosheets via edge-selective bonding of sacrificial C_{60} molecules. *Nat. Commun.* **9**, 4177–4186 (2018).
12. L. Li *et al.*, Black phosphorus field-effect transistors. *Nat. Nanotechnol.* **9**, 372–377 (2014).
13. Y. Zhao *et al.*, Surface coordination of black phosphorus for robust air and water stability. *Angew. Chem. Int. Ed. Engl.* **55**, 5003–5007 (2016).
14. S. Wu *et al.*, Black phosphorus: Degradation favors lubrication. *Nano Lett.* **18**, 5618–5627 (2018).
15. J. Sun *et al.*, A phosphorene-graphene hybrid material as a high-capacity anode for sodium-ion batteries. *Nat. Nanotechnol.* **10**, 980–985 (2015).
16. X. Huang, Z. Zeng, H. Zhang, Metal dichalcogenide nanosheets: Preparation, properties and applications. *Chem. Soc. Rev.* **42**, 1934–1946 (2013).
17. Y. Liu *et al.*, Tailoring sample-wide pseudo-magnetic fields on a graphene-black phosphorus heterostructure. *Nat. Nanotechnol.* **13**, 828–834 (2018).
18. L. Mao *et al.*, Stiffening of graphene oxide films by soft porous sheets. *Nat. Commun.* **10**, 3677 (2019).
19. M. Qiu *et al.*, Novel concept of the smart NIR-light-controlled drug release of black phosphorus nanostructure for cancer therapy. *Proc. Natl. Acad. Sci. U.S.A.* **115**, 501–506 (2018).
20. J. Song *et al.*, Advanced sodium-ion battery anode constructed via chemical bonding between phosphorus, carbon nanotube and crosslinked polymer binder. *ACS Nano* **9**, 11933–11941 (2015).
21. H. Ni *et al.*, Robust bioinspired graphene film via π-π cross-linking. *ACS Appl. Mater. Interfaces* **9**, 24987–24992 (2017).
22. P. Nakhanivej *et al.*, Revealing molecular-level surface redox sites of controllably oxidized black phosphorus nanosheets. *Nat. Mater.* **18**, 156–162 (2019).
23. I. K. Moon, J. Lee, R. S. Ruoff, H. Lee, Reduced graphene oxide by chemical graphitization. *Nat. Commun.* **1**, 73–79 (2010).
24. G. Zhou *et al.*, Oxygen bridges between NiO nanosheets and graphene for improvement of lithium storage. *ACS Nano* **6**, 3214–3223 (2012).
25. H. Hu *et al.*, Covalent functionalization of black phosphorus nanoflakes by carbon free radicals for durable air and water stability. *Nanoscale* **10**, 5834–5839 (2018).
26. H. J. Shin *et al.*, Efficient reduction of graphite oxide by sodium borohydride and its effect on electrical conductance. *Adv. Funct. Mater.* **19**, 1987–1992 (2009).
27. Y. Xu, H. Bai, G. Lu, C. Li, G. Shi, Flexible graphene films via the filtration of water-soluble noncovalent functionalized graphene sheets. *J. Am. Chem. Soc.* **130**, 5856–5857 (2008).
28. V. Georgakilas *et al.*, Noncovalent functionalization of graphene and graphene oxide for energy materials, biosensing, catalytic, and biomedical applications. *Chem. Rev.* **116**, 5464–5519 (2016).
29. K. W. Putz, O. C. Compton, M. J. Palmeri, S. T. Nguyen, L. C. Brinson, High-nanofiller-content graphene oxide-polymer nanocomposites via vacuum-assisted self-assembly. *Adv. Funct. Mater.* **20**, 3322–3329 (2010).
30. Y. Q. Li, T. Yu, T. Y. Yang, L. X. Zheng, K. Liao, Bio-inspired nacre-like composite films based on graphene with superior mechanical, electrical, and biocompatible properties. *Adv. Mater.* **24**, 3426–3431 (2012).
31. M. Zhang, L. Huang, J. Chen, C. Li, G. Shi, Ultratough, ultrastrong, and highly conductive graphene films with arbitrary sizes. *Adv. Mater.* **26**, 7588–7592 (2014).
32. R. Xiong *et al.*, Ultrarobust transparent cellulose nanocrystal-graphene membranes with high electrical conductivity. *Adv. Mater.* **28**, 1501–1509 (2016).
33. S. Keten, M. J. Buehler, Geometric confinement governs the rupture strength of H-bond assemblies at a critical length scale. *Nano Lett.* **8**, 743–748 (2008).
34. S. Park *et al.*, Graphene oxide papers modified by divalent ions-enhancing mechanical properties via chemical cross-linking. *ACS Nano* **2**, 572–578 (2008).
35. C. N. Yeh, K. Raidongia, J. Shao, Q. H. Yang, J. Huang, On the origin of the stability of graphene oxide membranes in water. *Nat. Chem.* **7**, 166–170 (2014).
36. K. Hu *et al.*, Written-in conductive patterns on robust graphene oxide biopaper by electrochemical microstamping. *Angew. Chem. Int. Ed. Engl.* **52**, 13784–13788 (2013).

37. H. Zhao, Y. Yue, Y. Zhang, L. Li, L. Guo, Ternary artificial nacre reinforced by ultrathin amorphous alumina with exceptional mechanical properties. *Adv. Mater.* **28**, 2037–2042 (2016).
38. J. Wang, J. Qiao, J. Wang, Y. Zhu, L. Jiang, Bioinspired hierarchical alumina–graphene oxide–poly(vinyl alcohol) artificial nacre with optimized strength and toughness. *ACS Appl. Mater. Interfaces* **7**, 9281–9286 (2015).
39. S. Gong *et al*., Integrated ternary bioinspired nanocomposites via synergistic toughening of reduced graphene oxide and double-walled carbon nanotubes. *ACS Nano* **9**, 11568–11573 (2015).
40. P. Ming *et al*., Nacre-inspired integrated nanocomposites with fire retardant properties by graphene oxide and montmorillonite. *J. Mater. Chem. A Mater. Energy Sustain.* **3**, 21194–21200 (2015).
41. G. He *et al*., Bioinspired ultrastrong solid electrolytes with fast proton conduction along 2D channels. *Adv. Mater.* **29**, 1605898 (2017).
42. S. Wan *et al*., Synergistic toughening of graphene oxide-molybdenum disulfide-thermoplastic polyurethane ternary artificial nacre. *ACS Nano* **9**, 708–714 (2015).
43. Y. Cheng, J. Peng, H. Xu, Q. Cheng, Glycera-inspired synergistic interfacial interactions for constructing ultrastrong graphene-based nanocomposites. *Adv. Funct. Mater.* **28**, 1800924 (2018).
44. S. Wan *et al*., Fatigue resistant bioinspired composite from synergistic two-dimensional nanocomponents. *ACS Nano* **11**, 7074–7083 (2017).
45. Y. Gao, H. Xu, Q. Cheng, Multiple synergistic toughening graphene nanocomposites through cadmium ions and cellulose nanocrystals. *Adv. Mater. Interfaces* **5**, 1800145 (2018).
46. S. Wan, F. Xu, L. Jiang, Q. Cheng, Superior fatigue resistant bioinspired graphene-based nanocomposite via synergistic interfacial interactions. *Adv. Funct. Mater.* **27**, 1605636 (2017).
47. S. Gong, Q. Zhang, R. Wang, L. Jiang, Q. Cheng, Synergistically toughening nacre-like graphene nanocomposites via gel-film transformation. *J. Mater. Chem. A Mater. Energy Sustain.* **5**, 16386–16392 (2017).
48. S. Gong, L. Jiang, Q. Cheng, Robust bioinspired graphene-based nanocomposites via synergistic toughening of zinc ions and covalent bonding. *J. Mater. Chem. A Mater. Energy Sustain.* **4**, 17073–17079 (2016).
49. S. Wan *et al*., Sequentially bridged graphene sheets with high strength, toughness, and electrical conductivity. *Proc. Natl. Acad. Sci. U.S.A.* **115**, 5359–5364 (2018).
50. Q. Zhang, S. Wan, L. Jiang, Q. Cheng, Bioinspired robust nanocomposites of cooper ions and hydroxypropyl cellulose synergistic toughening graphene oxide. *Sci. China Technol. Sci.* **60**, 758–764 (2017).
51. J. Duan *et al*., Bioinspired ternary artificial nacre nanocomposites based on reduced graphene oxide and nanofibrillar cellulose. *ACS Appl. Mater. Interfaces* **8**, 10545–10550 (2016).
52. S. Ye, B. Chen, D. Hu, C. Liu, J. Feng, Graphene-based films with integrated strength and toughness via a novel two-step method combining gel casting and surface crosslinking. *ChemNanoMat* **2**, 816–821 (2016).
53. S. Wan *et al*., Ultrastrong graphene films via long-chain π-bridging. *Matter* **1**, 389–401 (2019).
54. G. Xin *et al*., Microfluidics-enabled orientation and microstructure control of macroscopic graphene fibres. *Nat. Nanotechnol.* **14**, 168–175 (2019).
55. G. Xin *et al*., Highly thermally conductive and mechanically strong graphene fibers. *Science* **349**, 1083–1087 (2015).
56. J. Song *et al*., Processing bulk natural wood into a high-performance structural material. *Nature* **554**, 224–228 (2018).
57. F. Shahzad *et al*., Electromagnetic interference shielding with 2D transition metal carbides (MXenes). *Science* **353**, 1137–1140 (2016).
58. S. Luo *et al*., Self-standing polypyrrole/black phosphorus laminated film: Promising electrode for flexible supercapacitor with enhanced capacitance and cycling stability. *ACS Appl. Mater. Interfaces* **10**, 3538–3548 (2018).
59. J. Zhong *et al*., Efficient and scalable synthesis of highly aligned and compact two-dimensional nanosheet films with record performances. *Nat. Commun.* **9**, 3484–3495 (2018).
60. S. Xu *et al*., Flexible lithium–CO_2 battery with ultrahigh capacity and stable cycling. *Energy Environ. Sci.* **11**, 3231–3237 (2018).
61. H. Song *et al*., Hierarchically porous, ultrathick, "breathable" wood-derived cathode for lithium-oxygen batteries. *Adv. Energy Mater.* **8**, 1701203–1701210 (2017).